Journal of The
Electrochemical Society

Electrochemical Impedance Analysis and Modeling of Electrolyte Supported Solid Oxide Fuel Cells with LSM Air Electrodes

To cite this article: S. Golani *et al* 2025 *J. Electrochem. Soc.* **172** 064513

Journal of The Electrochemical Society, 2025 **172** 064513

Electrochemical Impedance Analysis and Modeling of Electrolyte Supported Solid Oxide Fuel Cells with LSM Air Electrodes

S. Golani,[z] Vignesh Umarani Renugopal, and A. Weber[*]

Institute for Applied Materials—Electrochemical Technologies (IAM-ET), Karlsruhe Institute of Technology (KIT), Karlsruhe, 76131, Germany

Lanthanum strontium manganite (LSM)-based air electrodes are applied in solid oxide cells for high-temperature operations (800 °C–1000 °C), offering chemical and microstructural stability despite relatively lower performance. This work focuses on impedance study of hexis electrolyte supported cells with LSM air electrodes and Nickel/Gadolinia-doped Ceria (Ni/GDC) fuel electrodes. Electrochemical impedance spectroscopy and distribution of relaxation times (DRT) were employed to analyze performance-limiting processes in single cells with a 1 cm^2 active electrode area. This analysis identified losses across five frequency ranges (5 DRT peaks), with no clear correlation to operating parameters. To deconvolute the processes and isolate loss mechanisms in both air and fuel electrodes, symmetrical cells were studied across a wide range of temperatures and air/fuel compositions. These measurements allowed for the separation of air and fuel electrode processes, development of a meaningful equivalent circuit model, and extraction of the model parameters using complex non-linear least squares fitting. These parameters were applied to build a 0-dimensional nonlinear DC performance model, which showed excellent agreement with the measured current-voltage data. The findings revealed that, in contrast to cells with mixed-conducting LSCF air electrodes, cell performance is limited by the LSM air electrode.

 [DOI: 10.1149/1945-7111/ade505]

Manuscript submitted January 26, 2025; revised manuscript received May 14, 2025. Published June 25, 2025.

List of symbols

Greek Symbols

α	Charge transfer coefficient (−)
γ	Exponential prefactor (Am^{-2})
η	Overpotential (V)
ψ	Microstructure parameter (−)
Δ	Deviation (−)

Subscripts

act	Activation
AE	Air Electrode
cell	Cell
corr	Correction
diff	Gas Diffusion
eff	Effective
EL	Electrode
FE	Fuel Electrode
H_2	Hydrogen
H_2O	Steam
He	Helium
load	Electrical load
N_2	Nitrogen
O_2	Oxygen
OCV	Open Circuit Voltage
ohm	Ohmic
pol	Polarization

Symbols

Al_2O_3	Aluminum Oxide
a	Exponent describing hydrogen partial pressure dependency of the fuel electrode´s exchange current density (−)
b	Exponent describing steam partial pressure dependency of the fuel electrode´s exchange current density (−)
B_{ohm}	Cell specific constant for ohmic resistance ($K\Omega^{-1}m^{-2}$)
B_{EL}	Cell specific constant for electrodes (Ωm^2)
D_{ijk}	Gas diffusion coefficient with the component i, j, k ($m^2\ s^{-1}$)
E	Activation energy ($Jmol^{-1}$)
EL	Electrode
F	Faraday constant (mol^{-1})
G_{eff}	Effective Gas Diffusion Parameter (m^{-1})
He	Helium
H_2	Hydrogen
H_2O	Steam
j	Current density (Am^{-2})
$j_{0,\ EL}$	Exchange current density (Am^{-2})
k_1, k_2, k_3	Polynomial coefficients
L	Diffusion length (m)
LSCF	$La_{0.6}Sr_{0.4}Co_{0.2}Fe_{0.8}O_{3-\delta}$
m	Exponent describing oxygen partial pressure dependency of the fuel electrode´s exchange current density (−)
N_2	Nitrogen
Ni/GDC	Nickel/Gadolinium-Doped Ceria
Ni/YSZ	Nickel/Yttria-Stabilized Zirconia
O_2	Oxygen
p	Overall pressure (atm)
p_{ref}	Reference pressure = atm
p_i	Partial pressure of the component
p_{corr}	Conversion factor ($Pa\ atm^{-1}$)
P_n	Peak number (−)
c_{xy}	Polynomial coefficients
R	universal gas constant ($Jmol^{-1}K^{-1}$)
R_{act}	Activation resistance (Ωm^2)
R_{diff}	Gas diffusion resistance (Ωm^2)
R_{ohm}	ohmic resistance (Ωm^2)
R_{pol}	Polarization resistance (Ωm^2)
ΔR_{diff}	Difference of the gas diffusion resistance (Ωm^2)
ΔR_{pol}	Difference of the polarization resistance (Ωm^2)
R_{load}	Load resistance (Ωm^2)
T	Temperature (K)
U_{OCV}	Open circuit voltage (V)
U_{cell}	Cell voltage (V)
z	Number of exchanged electrons (−)
6ScSZ	6 mol-% Scandia/Stabilized Zirconia

*Electrochemical Society Member.
[z]E-mail: sadhana.golani@kit.edu

Solid oxide fuel cells (SOFCs) are promising power generation systems that convert chemical energy into electrical energy. They have a high potential for efficient conversion of fuels, offer fuel flexibility, and enable combined heat and power generation.[1] To meet commercial requirements, development of this system requires detailed identification and understanding of electrodes and electrolyte processes in the fuel cell. Therefore, during the last decades, continuous advancement has led to various types of SOFC, differing in electrolyte and electrode materials, layer structure, and mechanically supporting layer. A typical SOFC comprises three essential components: a porous fuel electrode, a porous air electrode, and a dense electrolyte layer.

The most commonly used cell architecture in industrial applications is the electrolyte supported cells (ESCs), where the thick electrolyte layer provides the primary mechanical support for the entire cell structure. This design offers higher flexibility in applicable electrode materials, enabling a lower susceptibility towards anode re-oxidation, and strong mechanical support from the electrolyte layer.[2,3] This dense electrolyte effectively separates air and fuel, facilitates high ionic conductivity for the proper migration of oxygen ions, and acts as an electrical barrier, preventing electron flow between the air and fuel electrodes.[4] Zirconia is a leading choice for electrolytes, with yttria-stabilized zirconia (YSZ) being widely used. However, YSZ requires high operating temperatures (800 °C–1000 °C) to achieve adequate ionic conductivity, leading to degradation of SOFC components over time.[5] This has spurred the development of materials that offer sufficient conductivity in the intermediate temperature range (700 °C–850 °C) to reduce SOFC operating temperatures. Scandia-stabilized zirconia (ScSZ) exhibits the highest conductivity among zirconia-based electrolytes, making it a promising solution for lowering operating temperatures.[6]

In ESCs, using nickel/gadolinium doped ceria (Ni/GDC) fuel electrodes have become common for nearly two decades, as they reduce operating temperatures and minimize losses.[7–10] Compared to nickel/yttria-stabilized zirconia (Ni/YSZ) electrodes, Ni/GDC electrodes offer higher ionic and electronic conductivity, and a higher activity for oxygen exchange reactions on the oxide surface.[11] Additionally, ceria-based fuel electrodes are less degraded by Ni-agglomeration, offer good resistance to carbon deposition and sulfur poisoning, and enable a high redox stability.[12–15]

For the air electrode in SOFCs, lanthanum strontium manganite (LSM) perovskite is an important air electrode material. The performance of LSM-based electrodes is a complex function of composition, microstructure, electrode/electrolyte interface, and activation effect.[16,17] It offers excellent catalytic activity, and high chemical, thermal and mechanical stability.[17,18] These electrodes have a thermal expansion close to one of the electrolytes, which stabilizes and minimizes thermal stress in the cell and are therefore used for producing various electrodes.[19] However, due to the poor ionic conductivity of single phase LSM air electrodes, the active area for a catalytic reaction is limited to the triple phase boundaries (TPBs) on the electrolyte surface which is insufficient.[18,20] Hence, LSM-YSZ composite air electrodes, which perform significantly better given their larger utilization region,[21] have become state-of-the-art. To further enhance SOFC performance, the structure of LSM/YSZ has been optimized in such a way that TPBs within the electrode contribute to the reactions.[18]

While LSM-based composites have long been regarded as benchmark air electrode materials due to their excellent electronic conductivity and chemical stability in oxidizing environments, recent research has increasingly focused on LSCF ($La_{0.6}Sr_{0.4}Co_{0.2}Fe_{0.8}O_{3-\delta}$) as a preferred alternative, particularly for intermediate-temperature SOFCs (600 °C–800 °C). Although LSM has seen widespread application, studies specifically investigating its composite forms remain relatively limited; however, the available literature presents several noteworthy findings.

Mai et al. concluded that the degradation for fuel electrode supported cells (FESCs) with composite LSM is smaller than FESCs with LSCF air electrodes.[22] Tsai et al. also showed that the operating temperature range of SOFCs with LSM based air electrodes can be extended down to 700 °C.[23] Prestat et al. used State-Space Modelling to interpret impedance spectra and identify reaction mechanisms and kinetics at the LSM/YSZ interface for an electronic conducting air electrode.[24] The LSM air electrodes' electrocatalytic activity was analyzed at various oxygen partial pressures, overpotentials, temperatures, and electrode geometries for different cell configurations using electrochemical impedance spectroscopy (EIS) measurements by Barbucci et al.[25] Results revealed that microstructure of the electrode and operating conditions play a significant role in electrode performance and showed a dependency on electrode thickness, confirming that morphology plays a key role in the performance of electrodes in SOFCs.

A former company "Hexis AG" in Winterthur, Switzerland, developed a SOFC based μCHP-system featuring a radial repeat unit design exhibiting ESCs with LSM based air electrodes and Ni/GDC fuel electrodes.[26] During the cell and stack development process at "Hexis AG," various laboratory tests were done on the stack level to study performance and durability.[26–28] Valuable insights were attained at regular intervals using EIS to understand fundamental degradation mechanisms for long-term operation of SOFC stacks.[27,28] However, there is still a need to analyze this system at a finer level and attain detailed information. Hence, this work will focus on deconvoluting the losses and predicting the performance at a single cell level over a wide technically relevant SOFC operating range. In this study, an experimental approach using EIS combined with advanced modeling will be discussed for a comprehensive understanding of the ESC (Ni/GDC fuel electrode, LSM-based air electrode). Different loss mechanisms and their contributions will be identified and subsequently separated by means of distribution of relaxation times (DRT) in conjunction with fitting the measured spectra to a physicochemically meaningful equivalent circuit model (ECM). After determining ECM parameters, a zero-dimensional model for predicting the current-voltage (CV) characteristics of the ESC is applied, parameterized, and validated. Subsequently, a comparative assessment of different types of cells (FESCs/ESCs) with different electrolytes, fuel and air electrodes will be presented to examine variations in key parameters, and to demonstrate the model's predictive capability across different systems.

Experimental

Incremental 1 cm^2 ESCs, produced at "former Hexis AG" facility in Winterthur, were investigated in this study. The cell is exhibiting a Nickel/Gadolinia-doped Ceria (Ni/GDC) fuel electrode, a 6 mol-% Scandia/Stabilized Zirconia (6ScSZ) electrolyte and an LSM-based air electrode. To enhance the density of electrochemically active three phase boundaries for oxygen reduction reaction, an LSM-10Sc1CeSZ composite layer is applied as the active electrode layer. Additionally, a pure LSM layer is used as a current collector on the air side to decrease in-plane losses and enhance gas transport underneath the contact points in the stack. On the fuel side this is achieved by a Ni-contact layer and a Ni-mesh. To analyze the thickness and microstructure of different layers, the cell was examined using Scanning Electron Microscopy (SEM) as shown in Fig. 1. It is important to note that upon removal of the cell from the test setup, the Ni contact layer delaminates as it is sintered on the Ni contact mesh during operation.

The testing facilities used for electrochemical characterization of the cells are described in Ref. 29. To analyze single cells, an inert testing environment with ceramic flow fields and finely meshed contact grids was employed. The cells were mounted in a ceramic housing and gold frames were used for sealings. The fuel electrode was contacted by finely meshed nickel grids, similar to the configuration used in the Hexis stack whereas a gold mesh providing an ideal contacting was used at the air electrode. These contact-meshes provide a homogeneous current collection and uniform gas distribution across the entire electrode area. The combination of ceramic Al_2O_3 flow fields with contact meshes also mitigates the

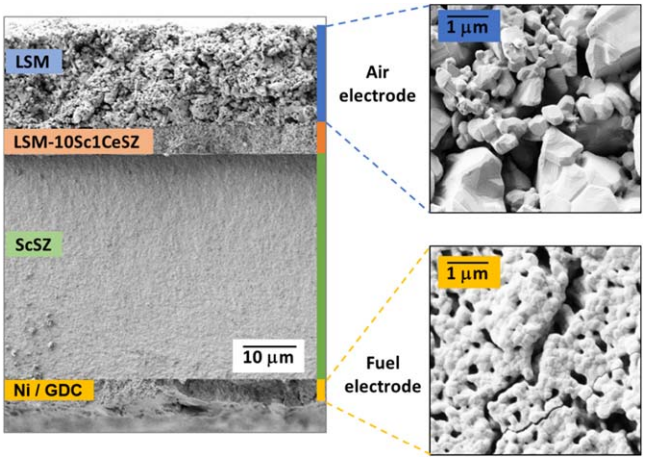

Figure 1. SEM image of cross section of a full cell (fuel electrode ~11 µm, electrolyte ~103 µm and air electrode ~57 µm) after testing. Secondary scattering electron detector, electron energy: 3 keV. The initially green Ni contact layer is sintered onto the Ni-mesh and thus delaminated during cell removal from the test bench.

possibility of any contact resistance due to corrosion as well as chromium poisoning of the air electrode. For reliable contacting, a contact force of 400 Ncm^{-2} using weights, was applied to each electrode. For symmetrical fuel and air electrode cells, appropriate contacting configurations were used on both sides.

To identify the composition and distribution of the large particles observed in the air electrode layer, energy-dispersive X-ray spectroscopy (EDS) analysis was performed on the cross-sectional region containing both the air electrode and the electrolyte. As shown in Fig. 2, the elemental maps of Sr, La, and Mn (Figs. 2d–2f) reveal concentrated regions consistent with the presence of the LSM phase, confirming that the large particles are LSM-rich. Moreover, due to the low concentration of Ce (1 mol%), it is not clearly detectable in the analysis. Additionally, the quantitative EDS table (Fig. 2j) provide the normalized weight and atomic percentages of all detected elements, averaged over multiple points, further confirming the phase distribution. These results support the identification of the air electrode as a composite of LSM and 10Sc1CeSZ.

For startup of the cells, a predefined heat up and reduction procedure was performed prior to the testing phase. All measurements were performed using the gas flow rate of 250 sccm per electrode, ensuring minimal fuel and oxidant utilization. As the active area is small, the lateral gradients in temperature and the current density as well as gas conversion were negligible. The symmetrical cells, which had similar electrode thickness, were tested in an identical setup with a total gas flow rate of 500 sccm provided to both electrodes.

The full cells were tested galvanostatically under ambient pressure with ambient air as the oxidant. The operating conditions were systematically varied by adjusting the fuel and oxidant gas mixtures via a gas mixing unit with Mass Flow Controllers (MFCs). At the fuel electrode various combinations of Hydrogen/Nitrogen/Oxygen ($H_2/N_2/O_2$) mixtures were used. The production of steam in the fuel was realized by feeding oxygen into a downstream combustion chamber. To study the gas diffusion processes, Helium (He) was used as an alternative inert gas at air as well as fuel electrode.[30] Additionally, to capture aging effects, reference measurements were conducted after each series of EIS measurements. This approach enabled the detection of changes in ohmic and polarization resistance, which are indicative of degradation during the test.

The detailed evaluation using EIS was performed under open-circuit conditions, except for the determination of charge transfer coefficients.[31] Impedance measurements were carried out in such a way that only one parameter at a time - either temperature or the partial pressures of fuel components (H_2, H_2O, N_2, He) or oxidant components (O_2, N_2, He)—was varied. The analysis aimed to thoroughly identify and assess contributions from the electrodes, electrolyte, and gas diffusion resistance, evaluating their impacts on the overall cell performance.

All the spectra were measured with a Solartron 1260 frequency response analyzer in a frequency range from 30 mHz to 1 MHz with 12 points per decade.[32] The current stimulus amplitude was adjusted to achieve a voltage response not higher than 12 mV. To ensure the validity of impedance spectra, the linear Kramers Kronig test was applied.[32] For impedance data analysis, DRT and subsequently Complex Non-Linear Least Square (CNLS) fitting were applied to separate and quantify the loss processes in the spectra. The optimal starting parameters for the CNLS algorithm used in the model are obtained through preidentification of the impedance response, achieved by calculating and analyzing the DRTs.[29]

Ideally, from the calculated DRTs, individual polarization losses would be identifiable as distinct peaks exhibiting a characteristic frequency. However, in the cells used in this study, the loss processes from the fuel and air electrode strongly overlap with each other in the spectrum. To address this, the analysis of symmetrical fuel and air electrode cells was used to deconvolute these overlapping processes. Subsequently, a physiochemically meaningful Equivalent Circuit Model (ECM) was developed, accounting for all the layers of the cell.

This model is a physically meaningful electrical equivalent circuit determined based on the DRT results.[33] With the help of this ECM the measured impedance spectra were separated into individual loss contributions, thus permitting a precise determination of the area-specific resistance values for the losses in the investigated cells. After quantifying the associated electrochemical losses, a zero-dimensional (0D) stationary cell model was parameterized based on the approach outlined in Refs. 29, 30. This model predicts the cell's performance across a wide range of operating conditions.

In conjunction with the EIS-measurements, the overall cell performance was determined using CV characteristics. To prevent enhanced aging, the measurements were conducted with the voltage limited to 0.6 V.

Results

This section discusses the electrochemical performance of the examined ESCs, featuring Ni/GDC fuel electrodes and LSM air electrodes.

In the first analysis, the impedance spectrum of the full cell is compared with those of symmetrical cells - exhibiting fuel or air electrodes on both sides of the supporting electrolyte, as well as reconstructed spectrum representing the combined (fuel + air) electrode, as shown in Fig. 3. To obtain the combined (fuel + air) electrode impedance, the real (Re(z)) and imaginary (Im(z)) components of the impedance spectra from the symmetrical fuel and air electrode cells are each divided by two and then summed. This approach estimates the total electrode contribution as if both electrodes were present on the same cell. The distribution of relaxation times (DRT) analysis was performed on the reconstructed (fuel + air) electrode spectrum and the results show good agreement with the full cell measurements with ideal contacting. The DRT results also reveal overlapping peaks associated with the fuel and air electrodes, further complicated by multiple peaks arising from the complex coupling of electronic, ionic, and gas-phase transport in the porous multiphase electrodes.[34] Thus, the simple approach of deconvoluting the fuel and air electrode, and electrolyte processes based on the DRT peaks is not effective.

At nominal operating temperatures of SOFCs (700 °C–900 °C), only electrode processes are detectable within the investigated frequency range of 0.1 Hz to 1 MHz.[34] It can be observed that peak 1 is mainly influenced by the fuel electrode, while peaks 2 to 4 are dominated by the air electrode. However, under different operating conditions (temperature, pO_2,AE, pH_2O,FE), this pattern

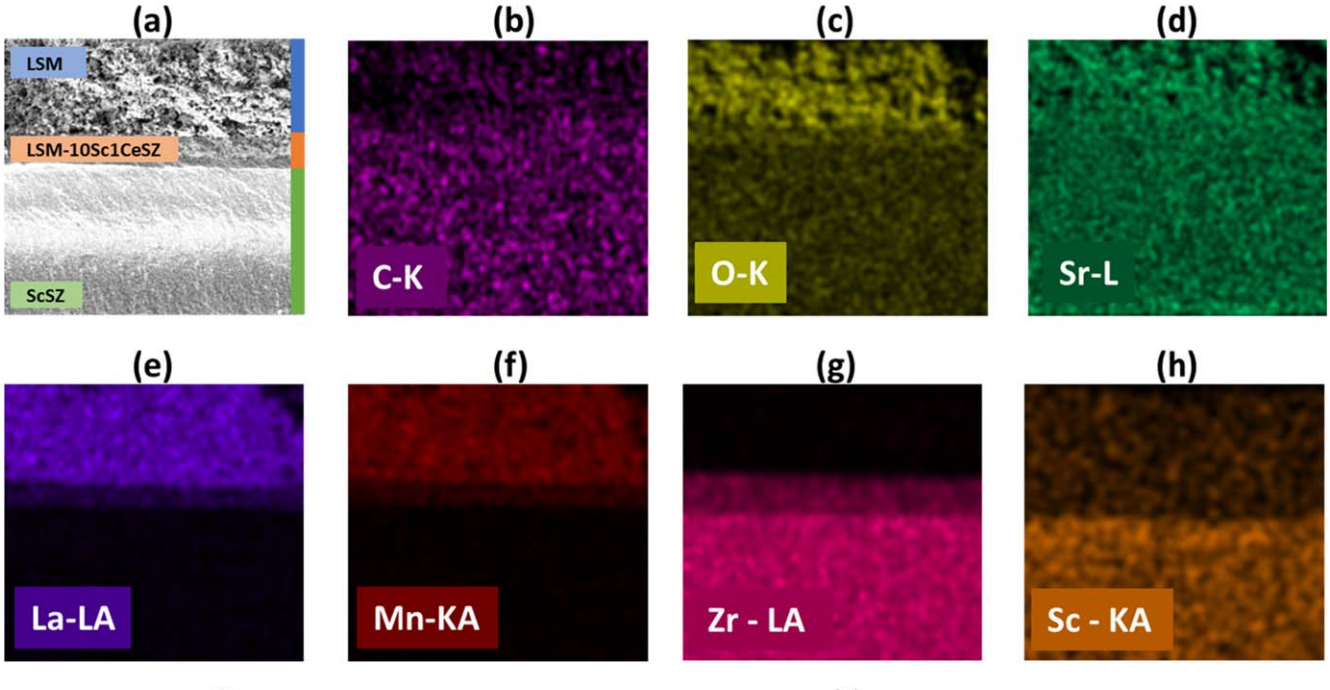

(j)

Element	Atomic Number	X-ray Series	Unnormalized concentration (Weight %)	**Normalized concentration (Weight %)**	Atomic concentration (Atomic %)	**Error (%)**
C	6	K	0.74	0.88	3.54	0.1
O	8	K	15.01	17.72	53.65	1.7
Sr	38	L	0.96	1.13	0.62	0.1
La	57	L	16.63	19.63	6.85	0.5
Mn	25	K	7.55	8.91	7.86	0.2
Zr	40	L	43.84	51.73	27.48	1.7
Ce	58	L	0.0	0.0	0.0	0.0
		Total	84.73	100	100	

Figure 2. Energy-dispersive X-ray spectroscopy (EDS) analysis of the cross-sectional region containing the air electrode and electrolyte (a) SEM image (b)–(h) EDS elemental maps indicating the distribution of C, O, Sr, La, Mn, Zr, and Sc respectively. (i) Composite map illustrating the heterogeneous distribution of all detected elements. (j) Elemental composition table summarizing the normalized weight percentages (%), atomic percentages (%), and associated measurement errors for each element. Values represent averages obtained from multiple points across the region analyzed.

does not always hold, and variations in peak sizes, as well as stronger overlaps, were observed as discussed in further sections.

To analyze electrolyte processes, ionic transport, and the grain and grain boundary conductivities of electrolytes, measurements must be conducted at lower temperatures, where relaxation frequencies shift into an accessible range.[34,35] At these temperatures, additional electrolyte processes become visible in the DRTs as the characteristic frequencies of thermally activated processes move to lower values. However, since low-temperature measurements fall outside the scope of this study, the processes occurring within the electrolyte layer are collectively treated as part of the cell's overall ohmic resistance.

The approach used in this study is based on the methodologies outlined by Leonide et al.[29] and Grosselindemann et al.,[30] with additional modifications to determine the charge transfer coefficients. Initial interpretations based on characteristic frequencies and deconvolution suggested contributions from gas diffusion, charge transfer reactions, and ionic transport in the GDC-ScSZ matrix. However, assigning the peaks to corresponding physio-chemical processes and quantifying the contributions from the fuel and air electrodes through sensitivity analysis of full cell spectra proved unfeasible. Therefore, the ECM fitting values from the full cell were not used for modeling Current-Voltage (CV) characteristics, as they include contributions from both electrodes. Henceforth, results and discussion of the DRT analysis for full cells are provided in appendix.

To deconvolute and quantify the contributions from each electrode and set up the model, activation and diffusion losses from symmetrical cells are used. This method enables a more accurate separation and quantification of electrochemical losses, offering clearer insights into polarization and transport processes at each electrode. The gas diffusion processes inherent in the SOFC electrodes are often obscured by overlapping polarization losses, making it challenging to accurately analyze the diffusion-related overpotentials. Thus, to address this, inert gas measurements are conducted, followed by studying the impact of varying operating parameters on the DRT peaks of the symmetrical fuel and air electrode spectra.

Gas diffusion polarization.—The gas diffusion process exhibits a $T^{0.5}$ temperature dependency,[36] however, all DRT-peaks in symmetrical cells (Fig. 5 and as well as full cells (Fig. A·1 in

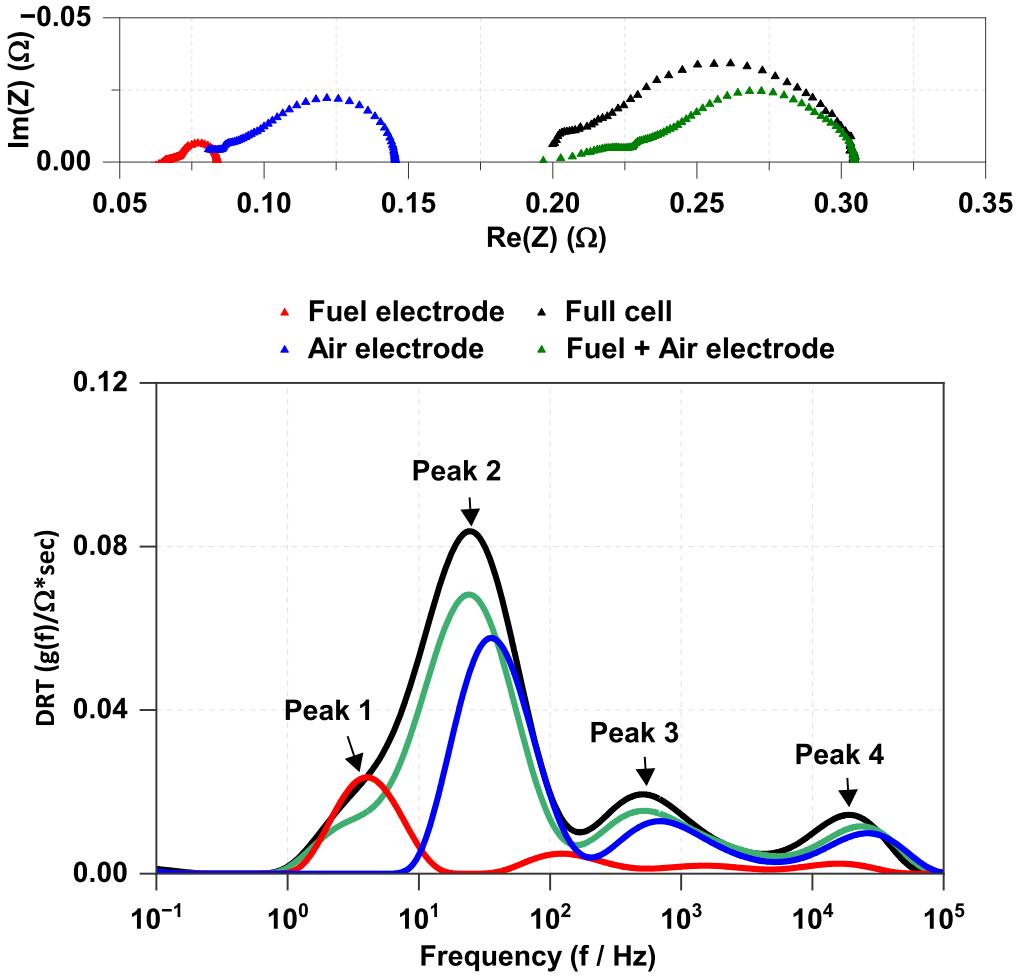

Figure 3. Impedance spectra (Nyquist plots) and DRT comparisons for symmetrical and full cells at 850 °C with 80% H_2 (balance H_2O) as fuel at the fuel electrode and synthetic air at the air electrode.

appendix) show a thermal activation. As a result, a direct correlation of gas diffusion with a single DRT-peak is not possible for either the fuel or air electrode. The observed peaks in the DRT suggest that gas diffusion processes are overshadowed by thermally activated electrochemical processes.

Hence, in order to deconvolute and quantify the gas diffusion process, a methodology based on inert gas variation previously applied to Ni/GDC fuel electrodes,[31] was applied to both fuel and air electrode. The difference in polarization resistances between two inert gases (N_2 & O_2, He & O_2) enables the quantification of gas diffusion resistance for various gas mixtures. Due to its temperature dependency and the thermal activation of other polarization contributions, gas diffusion becomes more pronounced and easier to resolve at higher temperatures. Thus, the analysis was performed at 900 °C for both fuel and air electrode[31] as shown in Fig. 4.

Since N_2 and He are electrochemically inactive, the difference in polarization resistance between the spectra is solely related to the different gas diffusion coefficients. Values of 0.023 Ωcm^2 and 0.009 Ωcm^2 were obtained for the fuel and air electrodes, respectively. As shown in Table I, similar values were obtained when the approach was applied to full cells. The relative deviation of ∼20% for the fuel electrode corresponds to an absolute error of 2 mΩcm^2, which is acceptable considering that the total resistance to be measured is roughly two orders of magnitude larger.

The difference in polarization resistances between these two inert gas components was used to determine an effective gas diffusion geometry parameter. This effective gas diffusion parameter (Eq. 1), which is the microstructural parameter (the porosity to tortuosity ratio of the electrode EL) divided by an effective diffusion length, allows for the calculation of the gas diffusion resistance for different temperatures and gas compositions according to Eqs. 2 and 3 for air and fuel electrodes, respectively.

$$G_{\text{eff,EL}} = \frac{\Psi_{\text{EL}}}{L_{\text{EL}}} \quad [1]$$

$$R_{\text{diff,AE}} = \left(\frac{\tilde{R}T}{4F}\right)^2 \cdot \frac{1}{G_{\text{eff, AE}}} \cdot \frac{1}{D_{O_2}} \left(\frac{1}{p_{O_2,\text{AE}}} - \frac{1}{p}\right) \cdot \frac{1}{P_{\text{corr}}} \quad [2]$$

$$R_{\text{diff,FE}} = \left(\frac{\tilde{R}T}{2F}\right)^2 \cdot \frac{1}{G_{\text{eff,FE}}} \cdot \left(\frac{1}{D_{H_2} \cdot p_{H_2,\text{FE}}} + \frac{1}{D_{H_2O} \cdot p_{H_2O,\text{FE}}}\right) \cdot \frac{1}{P_{\text{corr}}} \quad [3]$$

The calculated gas diffusion resistances at 900 °C are 0.0029 Ωcm^2 for the fuel electrode operated with an 80% H_2 (20% H_2O) fuel mixture and 0.0021 Ωcm^2 for the air electrode in air (21% O_2). Due to the abovementioned temperature dependency of gas diffusion, the gas diffusion polarization resistance will decrease further with decreasing temperatures and, according to Eq. 3, will increase with increasing hydrogen or steam concentrations. Moreover, when the inert gas mixture is replaced with a more realistic fuel and oxidant, the gas diffusion losses are reduced.[3]

After determination of the gas diffusion parameters Geff, the gas diffusion overpotentials were calculated by combining the Nernst-

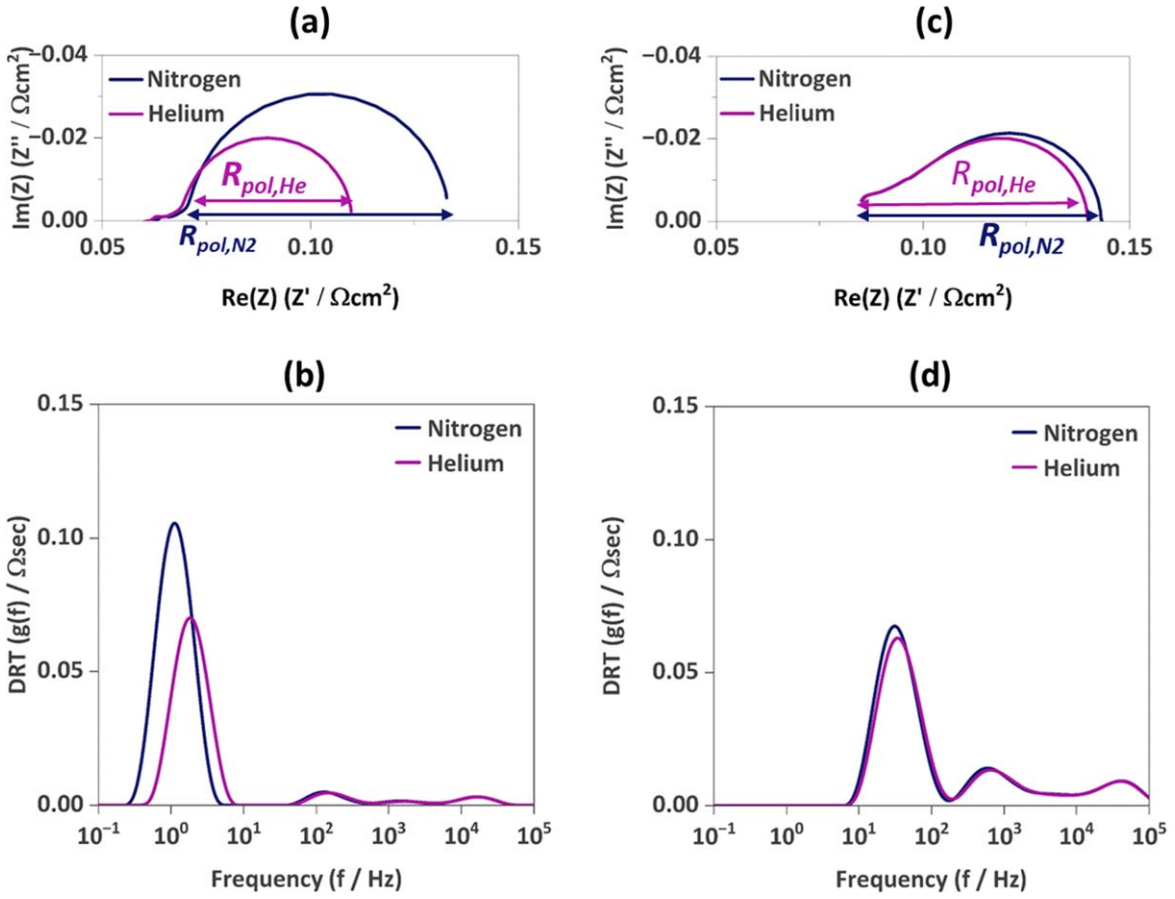

Figure 4. Impedance spectra (Nyquist plots) and DRT comparisons for symmetrical cells at 900 °C with two ternary gas mixtures using N_2 and He as inert gases. (a) Impedance spectra and (b) DRT for Symmetrical Ni/GDC fuel electrodes with 10% H_2, 5% H_2O and 85% N_2/He (c) Impedance spectra and (d) DRT for Symmetrical LSM air electrodes with 5% O_2 and 95% N_2/He.

Table I. Polarization resistance difference for all three types of cells.

Cell	Gas composition	Temp (°C)	Δ Rpol (=Δ rdiff) (Ωcm²)
Sym FE	10% H_2, 5% H_2O, 85% N_2/He	900	0.023
Sym AE	5% O_2, 95% N_2/He	900	0.009
Full Cell	FE: 10% H_2, 5% H_2O, 85% N_2/He AE: Air	890	0.023
Full Cell	AE: 5% O_2, 95% N_2/He FE: 95% H_2, 5% H_2O	900	0.011

Equation and Fick´s law of diffusion in Eqs. 4 and 5 for air and fuel electrodes, respectively.

$$\eta_{\mathrm{diff,AE}} = -\frac{\tilde{R}T}{4F}\ln\left(1 - \frac{\tilde{R}T(1 - p_{\mathrm{O_2,AE}}/p)}{4F\mathrm{Geff_{AE}}D_{\mathrm{O_2}}p_{\mathrm{O_2,AE}}P_{\mathrm{corr}}}\cdot j\right) \quad [4]$$

$$\eta_{\mathrm{diff,FE}} = \frac{\tilde{R}T}{2F}\ln\left(\frac{1 + \frac{\tilde{R}T}{2F\mathrm{Geff_{FE}}D_{\mathrm{H_2O}}p_{\mathrm{H_2O,FE}}P_{\mathrm{corr}}}\cdot j}{1 - \frac{\tilde{R}T}{2F\mathrm{Geff_{FE}}D_{\mathrm{H_2}}p_{\mathrm{H_2,FE}}P_{\mathrm{corr}}}\cdot j}\right) \quad [5]$$

Temperature variation in symmetrical cells.—Figure 5 shows the impact of operating temperature on the DRT of the fuel electrode (for different fuel gas compositions (a) and (b)) and the air electrode (c) and (d). Both fuel and air electrode each exhibit four distinct peaks in the DRT, with the main peak for each electrode occurring in the frequency range of 1 to 100 Hz. Since detailed microstructural and compositional. parameters required for more complex ECMs based on transmission line models (TLMs) of the electrodes are missing, equivalent circuits for the air and fuel electrodes are modeled using an appropriate number of four RQ elements each for further impedance data analysis.

For symmetrical fuel electrodes as shown in Figs. 5a and 5b, DRTs can be divided into three major groups P1A, P2A and (P3A +P4A). The analysis of different gas compositions revealed a distinct behavior for P1A at higher temperatures. The polarization resistance, encompassing all four peaks (P1A to P4A), increases with decreasing temperature, except for P1A at high temperatures and high hydrogen content (80%), as shown in Fig. 5b. This peak shift of P1A towards higher frequencies is also unexpected, as an increase in resistance would typically shift the relaxation frequency of an RC-element to lower frequencies. However, this behavior was also observed for Ni/GDC fuel electrodes at elevated temperatures before in Refs. 30, 37, 38. Thus, this overlap can be attributed to the interplay between gas diffusion and activation polarization at the fuel electrode. As shown in Fig. 4, the Ni/GDC fuel electrode exhibits significant gas diffusion in the frequency range of 1–10 Hz, suggesting that gas diffusion dominates in the first peak (P1A). These findings highlight that the share of gas diffusion becomes

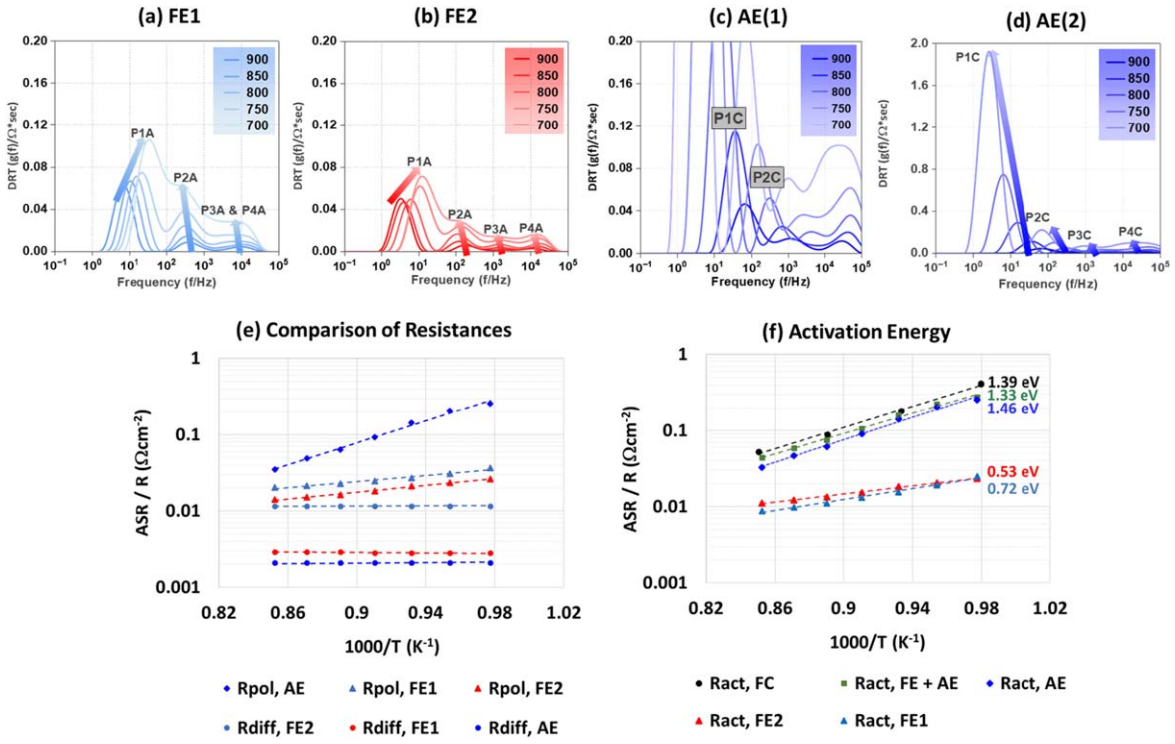

Figure 5. DRTs of impedance spectra of symmetrical cells in a temperature range from 900 °C to 700 °C (a) Ni/GDC fuel electrode 1 (FE1) with the fuel gas composition of 10% H_2, 40% H_2O and 50% N_2 (b) Ni/GDC fuel electrode 2 (FE2) with the fuel gas composition of 80% H_2 (balance H_2O) (c & d) LSM air electrode (with different $\langle i\rangle y\langle i\rangle$-axis) with synthetic air as an oxidant. This adjusted scaling in 4c reveals contributions of individual processes that appear suppressed in 4 d due to its compressed $\langle i\rangle y\langle i\rangle$-axis. (e) Comparison of polarization (R_{pol}) and diffusion (R_{diff}) resistances on a logarithmic scale for Ni/GDC fuel electrode 1 (FE1), Ni/GDC fuel electrode 2 (FE2) and LSM air electrode in a temperature range from 900 °C to 750 °C. (f) Comparison of activation energies (R_{pol}–R_{diff}) using Arrhenius-Plots for an ESC full cell, FE+AE and symmetrical cells with Ni/GDC fuel electrode FE1, FE2 and LSM air electrode in a temperature range from 900 °C to 750 °C.

more pronounced at higher temperatures, significantly impacting electrochemical processes and causing the peak P1A to shift towards higher frequencies.

With all other fuel electrode properties held constant during the DRT analysis, two major resistance peaks were identified: one at low frequency and one at medium frequency. Gas diffusion analysis revealed that the low-frequency peak includes both diffusion and other electrochemical processes, implying coupling of these processes at low frequencies. Similarly, for lower H_2 content, two peaks (P3A and P4A) overlap at higher frequencies. From this, it can be inferred that P1A includes gas diffusion contributions, while P2A and the combined P3A+P4A peaks reflect electrochemical processes, ionic transport, and contributions from GDC/ScSZ interfaces. The sum of P2A and P3A represents the overall activation polarization related to the coupling of charge transfer and transport in the Ni/GDC electrode, while P4A is associated with interfacial processes. Based on these analyses with varying compositions, along with four RQ elements and one ohmic resistor was employed.

To characterize the air electrode, impedance measurements were performed using ambient air as the oxidant. A significantly larger low-frequency peak was observed, likely corresponding to charge transfer resistance at the electrode–electrolyte interface and plays a central role in defining the overall impedance behaviour. As illustrated in Fig 5d, the DRTs of the LSM-based air electrode exhibit four distinct, thermally activated peaks and hence are effectively modelled using four RQ elements in the ECM. Further insight is provided by the DRTs obtained under inert gas conditions, shown in Fig. 4b, which indicate that gas diffusion in the air electrode primarily occurs within the 10–100 Hz frequency range. The ECM provided a good fit for experimental data and enabled reliable extraction of electrochemical parameters for the air electrode.

Understanding this behaviour is critical for interpreting impedance spectra and DRTs accurately. At higher temperatures, the low-frequency peak (1–10 Hz) is typically attributed to the fuel electrode, while at lower temperatures, it shifts toward the air electrode. Interestingly, at 800 °C, the dominant peaks of the fuel and air electrodes overlap at approximately 20 Hz, emphasizing the importance of frequency-dependent analysis for proper electrode characterization.

Activation polarization.—The equivalent circuit models as discussed above assisted in experimentally determining the resistance of activation polarization at different operating parameters under open-circuit conditions. The polarization resistance, R_{pol}, was determined by summing up the extracted resistances from the CNLS fit. This accounts for the polarization losses related to the coupling of charge transfer and ionic transport in the respective electrode. Electronic contributions in these electrodes are negligible because both nickel and LSM exhibit high electronic conductivities, exceeding the ionic conductivities of the electrolyte phases in the composite electrodes. Furthermore, current collector layers are applied, ensuring negligible in-plane electronic transport losses. Mass transport losses are excluded, as the gas diffusion polarization resistances are independently determined, and gas conversion is prevented by the cell geometry and the high gas flow rates. To calculate the activation energy of the electrodes, the computed gas diffusion resistances, R_{diff}, according to Eqs. 2 and 3, and as shown in Fig. 5e, were subtracted from R_{pol} according to Eq. 6. After these calculations, the temperature dependent activation polarization resistance ($R_{act,EL}$) was plotted and fitted to an Arrhenius model, according to Eq. 7 (Fig. 5f).

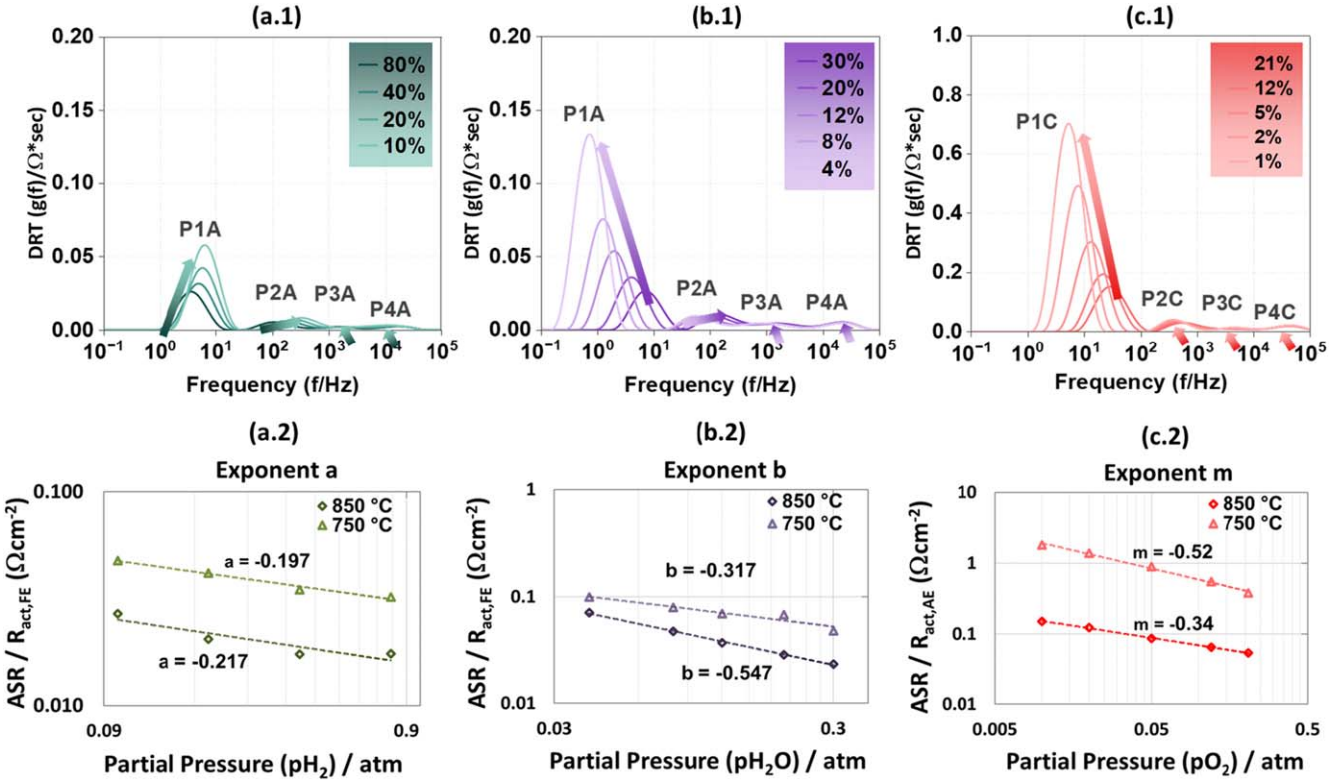

Figure 6. DRTs of impedance spectra of symmetrical Ni/GDC fuel and LSM air electrode cells at 850 °C with the with the fuel gas compositions of H_2, H_2O, N_2 (balancing inert gas) for the variation (a.1) pH_2 from 80% to 10%, 20% H_2O (rest N_2) (b.1) pH_2O from 30% to 4%, 60% H_2 (rest N_2) (c.1) pO_2 from 21% to 1% (rest N_2). Determination of the exponent a (a.2), b (b.2) and m (c.2) as a function of H_2, H_2O, O_2 partial pressure on a double-logarithmic scale, at temperatures 850 °C and 750 °C using the values of a single Ni/GDC fuel and LSM air electrode.

$$R_{act} = R_{pol} - R_{diff} \quad [6]$$

$$R_{act,\,EL}(T) = B \cdot \exp\left(\frac{E_{act}}{\tilde{R}T}\right) \quad [7]$$

Activation energy.—For the full cell, R_{act} follows a linear trend, resulting in an activation energy of 1.39 eV (80% H_2) in the Arrhenius diagram in Fig. 5f. Similarly, the temperature-dependent overall polarization resistance for the fuel electrode ($R_{pol,FE}$) and air electrode ($R_{pol,AE}$) are also displayed in Fig. 5e. The Arrhenius fit yields activation energies of 0.53 eV (80% H_2) for the fuel electrode and 1.46 eV for the air electrode. The results indicate that the activation energy of the air electrode is significantly higher than that of the fuel electrode. For symmetrical Ni/GDC electrodes, the activation energy of 0.47 eV and 0.94 eV was also reported in the literature corresponding to different rate-limiting processes occurring at Ni/GDC interface under varying conditions.[13,30] The lower value is typically attributed to surface-related processes, while the higher value reflects bulk diffusion or charge transfer mechanisms. Moreover, previous studies have highlighted the activation energy for the oxygen surface exchange process at the surface of the LSM electrodes ranged from 1.4 to 2 eV, with the results of this study aligning well with those values.[39–41] Considering the complexity of LSM/doped zirconia composite electrodes, the activation polarization might change depending on composition, microstructure and dopant levels. In the cell analyzed in this study, the LSM air electrode contributes significantly to the overall polarization resistance, exhibiting a higher activation energy. A detailed comparison with literature data, also tested previously in a similar setup is given in Table V.

Partial pressure variation in symmetrical cells.—The commonly used approach of temperature variation, which uniquely assigns a peak at a specific frequency to a particular electrochemical process, can lead to errors, especially when there is significant overlap between the peaks. To improve accuracy, the partial pressure variation at both fuel and air electrode was conducted and is discussed in this section. The partial pressures of reactants and reaction products were varied independently by applying the required amount of inert gas (N_2) to the fuel gas mixture. The measurements were done at two different temperatures (850 °C and 750 °C) and the DRTs of impedance spectra for 850 °C are shown in Figs. 6a.1, 6b.1 and 6c.1.

Exchange current density.—These partial pressures of the gaseous reactants ($p_{H2,FE}$, $p_{O2,FE}$), reaction products ($p_{H2O,FE}$), and temperature assist in calculating the exchange current densities for fuel and air electrodes as shown in Eqs. 8 and 9. Determining these values for full cells is particularly challenging, as they strongly depend on the specific cell configuration and electrode materials.[42,43] Since the required impedance measurements can be carried out under open circuit conditions, symmetrical cells are used. The dependencies of the operating parameters are described by a semi-empirical approach, which incorporates power functions for the partial pressures and Arrhenius-type temperature dependencies.

$$j_{0,FE} = \gamma_{FE}\left(\frac{p_{H_2,FE}}{p_{ref}}\right)^a\left(\frac{p_{H_2O,FE}}{p_{ref}}\right)^b \exp\left(-\frac{E_{act,FE}}{\tilde{R}T}\right) = \frac{1}{R_{act,FE}}\cdot\frac{RT}{2F} \quad [8]$$

$$j_{0,AE} = \gamma_{AE}\left(\frac{p_{O_2,AE}}{p_{ref}}\right)^m \exp\left(-\frac{E_{act,AE}}{\tilde{R}T}\right) = \frac{1}{R_{act,AE}}\cdot\frac{RT}{2F} \quad [9]$$

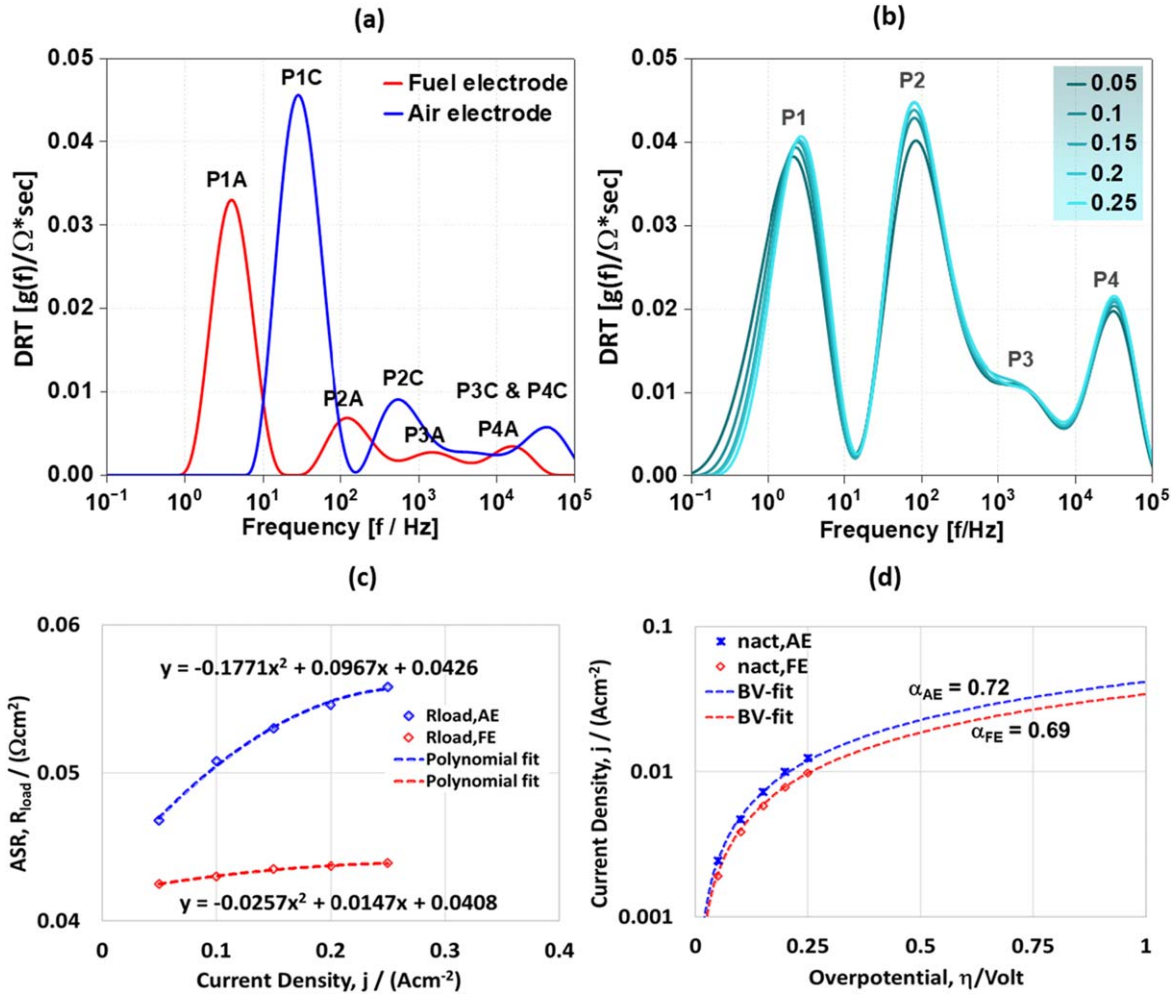

Figure 7. (a) Comparison of DRTs of impedance spectra of symmetrical Ni/GDC fuel electrode (80% H_2, balance H_2O) and LSM air electrode (pure O_2) at 850 °C. (b) DRT of the variation of the electrical load with a fuel gas mixture of 80% H_2 (balance H_2O) with pure O_2 at the air electrode at T = 850 °C. (c) Resistance ($R_{load,\ AE}$ and $R_{load,\ FE}$) as a function of the current density along with the two 2nd-order polynomial fits in with a fuel gas mixture of 80% H_2 (balance H_2O) with pure O_2 at the air electrode at T = 850 °C. (d) Determination of the charge transfer coefficient (α) in SOFC with a fuel gas mixture of 80% H_2 (balance H_2O) with pure O_2 at the air electrode at T = 850 °C (current density j as a function of activation overpotential $\eta_{act,\ FE}$ and $\eta_{act,\ AE}$ along with Butler-Volmer fits).

Seven unknown parameters can be identified from Eqs. 8 and 9: the activation energies $E_{act,FE}$ and $E_{act,AE}$, the dimensionless exponents: a, b and m, and the prefactors: γ_{FE} and γ_{AE}. Activation energies were determined from the activation polarization resistances, $R_{act,EL}$, (Eq. 7) as described in[31] and as discussed in section 4 based on the temperature-dependent behavior. The remaining parameters are calculated by varying the partial pressure of the gases.

Exponents: a, b and m.—The exponents a and b were determined by varying the partial pressure of H_2 and H_2O, respectively, using symmetrical fuel electrode cells. The partial pressures of the reactants and reaction products were varied independently introducing the required amount of inert gas (N_2) to the fuel gas mixture. Literature has shown that the exponents a and b are significantly dependent on temperature for Ni/GDC fuel electrodes.[30] Therefore, measurements were conducted at two different temperatures (850 and 750 °C). The resulting DRTs of the impedance spectrum for 850 °C, along with the dependencies, and the exponents a and b are shown in Figs. 6a.1, 6b.1, 6a.2 and 6b.2.

Similarly, the parameter m, which describes the dependence of the O_2 partial pressure on the air electrode's exchange current density, was determined using the equivalent circuit fitting data from open-circuit impedance measurements of symmetrical cells. This was done by varying p_{O2} at the air electrode, as shown in the DRTs in Fig. 6c.1. The resulting activation polarization resistance at two different temperatures (850 and 750 °C), using the Area Specific Resistance (ASR) values of a single air electrode, was plotted on a double logarithmic scale as a function of the oxygen partial pressure (p_{O2}) and fitted with a power law approach yielding the exponent m.

These exponents accurately reproduce the impact of partial pressures. However, in comparison to Ref. 31, the values for pH_2O- (fuel electrode) and pO_2-dependency (air electrode) show a significant temperature dependence. Since a detailed evaluation over a wide temperature range was not possible, the spectra were measured at two different temperatures, 850 and 750 °C and the corresponding values for a, b and m were calculated. For the 0D model, these values were linearly interpolated for the remaining temperatures. Therefore, a more comprehensive investigation of the temperature dependent behaviour is required for more precise calculations.

Prefactors: γFE and γAE.—The exponent and temperature dependent parameters, prefactor γ_{FE} and γ_{AE} can be derived from Eqs. 10 and 11. The calculation was performed after determining the exponents a, b, m, and using the cell constants B_{FE} and B_{AE} (obtained from the linear fits for the symmetrical fuel and air

Table II. Exponential Prefactors with the with an overall pressure of 1 atm at 850 °C.

Cell	Sym FE	Sym AE
Temperature (°C)	850 (1123.15 K)	850 (1123.15 K)
Partial Pressure (atm)	$pH_2 = 0.8$, $pH_2O = 0.2$	$pO_2 = 0.21$
Exponents (a, b, m)	a = −0.217 b = −0.547	m = −0.34
Cell specific constant (B/Ωm^2)	$B_{FE} = 5.74{\cdot}10^{-9}$ Ωm^2	$B_{AE} = 1.68{\cdot}10^{-12}$ Ωm^2
Prefactor (γ)	$=3.31{\cdot}10^{6}$ Am^{-2}K^{-1}	$=4.9{\cdot}10^{10}$ Am^{-2}K^{-1}

Table III. List of processes identified from the DRT analysis, together with their characteristic frequency range and dependencies at 850 °C. (+) Major (–) Minor dependency/contribution.

2.1 Fuel Electrode ($H_2 \rightarrow 2H^+ + 2e^-$)			
DRT peaks (Process)	Frequency range (Hz)	Dependencies	Contribution/physicochemical origin
P1A	10^0–10^1	Temperature (+) Gas diffusion (+)	Gas composition (+) Electrochemistry—Hydrogen oxidation (HOR) (+)
P2A	10^1–10^3	Temperature (+) Gas composition (+)	Electrochemistry
P3A & P4A	10^3–10^5	Temperature (−) Gas composition (−)	Ionic transport (electrolyte/interfacial processes)
2.2 Air Electrode ($1/2\,O_2 + 2e^- \rightarrow O^{2-}$)			
DRT peaks (Process)	Frequency range (Hz)	Dependencies	Contribution
P1C	10^1–10^2	Temperature (+) Gas diffusion (−)	Gas composition (+) Electrochemistry—Oxygen reduction (ORR) (+)
P2C	10^2–10^3	Temperature (+) Gas composition (−)	Electrochemistry (−)
P3C & P4C	10^3–10^5	Temperature (−) Gas composition (−)	Ionic transport (electrolyte/interfacial processes)
2.3 Full cell			
DRT peaks (Process)	Frequency range (Hz)	Convoluted Processes	
P1	10^0–10^1	P1A - Only visible at high H_2 concentrations ($pH_2 > 90\%$)	
P2	10^1–10^2	P2A (−) & P1C (+)	
P3	10^2–10^3	P2A (−), P3A (−) & P2C (+)	
P4 & P5	10^3–10^5	P3A, P4A, P3C & P4C	

electrodes). The same partial pressures used for the measurements and for the calculation of activation energies were applied in the computation.

$$\gamma_{FE} = \frac{\tilde{R}T}{2FB_{FE}} \cdot \left[\left(\frac{p_{H_2,FE}}{p_{ref}} \right)^a \left(\frac{p_{H_2O,FE}}{p_{ref}} \right)^b \right]^{-1} \quad [10]$$

$$\gamma_{AE} = \frac{\tilde{R}T}{2FB_{AE}} \cdot \left[\left(\frac{p_{O_2}}{p_{ref}} \right)^m \right]^{-1} \quad [11]$$

The values for these parameters reported in Ref. 31 vary by up to two orders of magnitude, making direct comparison difficult. Considering the influence of the parameters a, b, and m, the calculation of the prefactors for 850 °C, with an overall pressure of Pref = 1 atm is shown in Table II.

Activation overpotential.—A generalized Butler-Vomer approach is applied to correlate activation overpotential with current density. In our approach the Butler-Volmer (Eq. 12) does not treat electrode polarization as a single rate-determining step but instead considers it as the result of coupled charge transfer and ionic transport losses. Of the two unknown parameters identified in Eq. 12, the exchange current density ($j_{0,\,EL}$) was discussed and calculated in the previous section, while the charge transfer coefficient (α_{EL}) is discussed below.

$$j = j_{0,EL} \left[\exp\left(\alpha_{EL} \frac{zF\eta_{act,EL}}{\tilde{R}T} \right) - \exp\left(-(1 - \alpha_{EL}) \frac{zF\eta_{act,EL}}{\tilde{R}T} \right) \right] \quad [12]$$

*Charge transfer coefficients: αFE and αAE.—*The charge transfer coefficient (α) of the electrodes is used to describe the differences between forward and reverse behaviors of an electrochemical reaction and appears in the Butler-Volmer Eq. 12.

Since charge transfer coefficients cannot be determined from impedance spectra measured under open circuit conditions or from symmetrical cells in a polarized state, impedance spectra of full cells in polarized states are required for their calculation. The corresponding DRTs for different current densities are shown in Fig. 7. As discussed previously, the DRT peaks for fuel and air electrode overlap in the spectrum for the ESC cell used in this study. Hence, to calculate the coefficients separately for the fuel and air electrodes, operating conditions were chosen to enable a reasonable separation of the contributions from the fuel and air electrodes.

From Fig. 7a, it can be seen that there is no contribution from the air electrode below 10 Hz, and only minor contributions from the fuel electrode above 10 Hz at the selected operating point. Based on

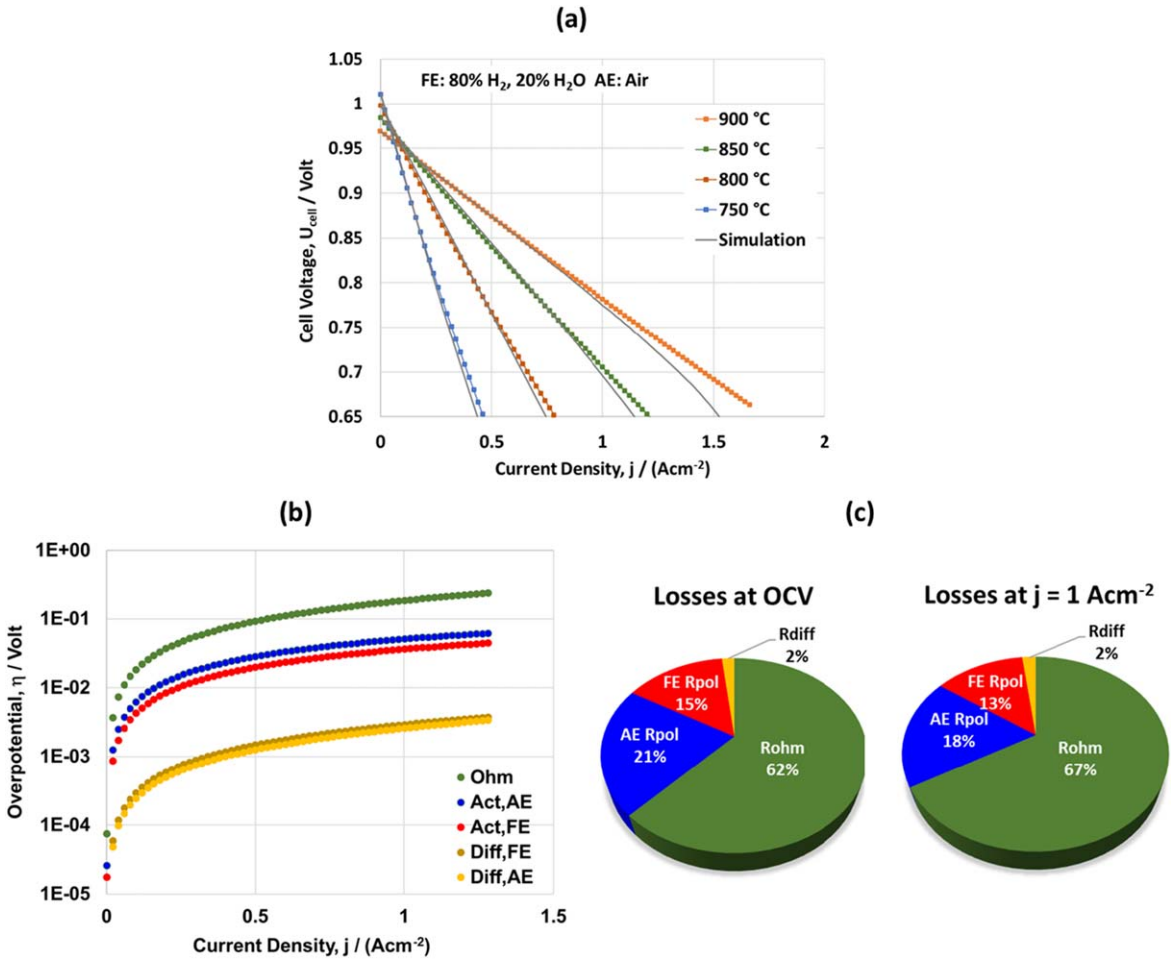

Figure 8. (a) Simulated CV curves using model parameters compared to measured CV curves at different temperatures with a fuel gas mixture of 80% H_2 (balance H_2O) and air as the oxidant. (b) Absolute overpotential values as a function of the current density j. (c) Contribution (%) of different losses under open circuit conditions and current density of j = 1 Acm^{-2} with a fuel gas mixture of 80% H_2 (balance H_2O) and air as the oxidant at 850 °C.

Table IV. Information about three different types of cells (similar electrodes, with similar thickness, are used for symmetrical cell analysis).

Type of cell Parameter	ESC A investigated cell Material and thickness	ESC B see[30] Material and thickness	FESC see[29] Material and thickness
Fuel Electrode	Ni/GDC ~11 μm	Ni/GDC ~24 μm	Ni/8YSZ Substrate ~1.5 mm Functional layer ~10 μm
Air Electrode	LSM/composite ~57 μm	LSCF ~30 μm	LSCF ~45 μm
Electrolyte	6ScSZ ~103 μm	3YSZ ~85 μm	8YSZ ~10 μm

this understanding, for symmetrical fuel electrodes, the resistance values derived from the CNLS fit of the equivalent circuit below 10 Hz for the full cell are directly considered for the polarization contribution of the fuel electrode.

To calculate the charge transfer coefficient, both symmetrical cells and full cells in the polarized state are used to determine the polarization resistance for the fuel and air electrodes. A fuel gas mixture of 80% H_2 (balance H_2O) was used with pure O_2 as the oxidant to avoid gas diffusion losses at the air electrode. The load current density was increased stepwise, from 0.05 A cm^{-2} to 0.25 A cm^{-2} at 850 °C. In the DRTs, shown in Fig. 7b, three main peaks in the lower and middle frequency ranges are summarized as $R_{load,FE}$, where P1 (~P1A) and small fractions of P2 and P3 (~P2A and P3A), are used from symmetrical fuel electrodes. These processes, which exhibit minor current density dependency, are considered for the fuel side, while the remaining peaks from the DRTs of the full

(Cells)

Parameter	Investigated cell	ESC [30]	FESC [29]
Type	ESC_A	ESC_B	FESC
Operating Temperature	850 °C	850 °C	750 °C
Fuel Electrode	Ni/GDC ~ 11 μm	Ni/GDC ~ 24 μm	Ni/8YSZ ~ 10 μm
Air Electrode	LSM/comp ~ 57 μm	LSCF ~ 30 μm	LSCF ~ 45 μm
Electrolyte	6ScSZ ~ 103 μm	3YSZ ~ 85 μm	8YSZ ~ 1.5 mm

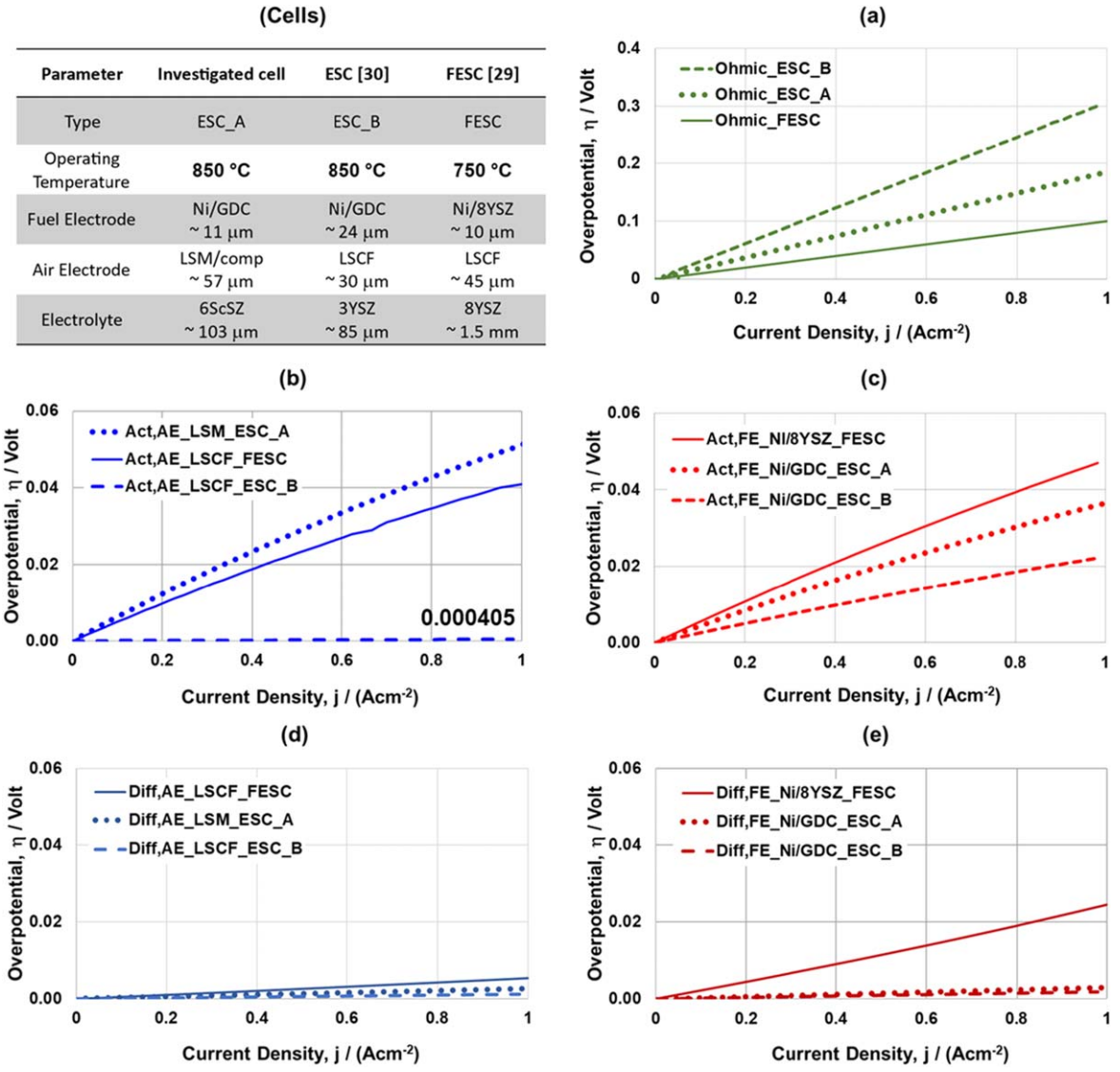

Figure 9. Comparison of absolute overpotential values as a function of the current density for three cells (Investigated cell, ESC,[30] FESC[29]) with a fuel gas mixture of 80% H_2 (balance H_2O) and air as the oxidant at the nominal operating temperature i.e. 850 °C for ESCs and 750 °C for the FESC. (a) Ohmic losses (b) Activation losses for air electrode (c) Activation losses for fuel electrode (d) Gas diffusion losses in the air electrode (e) Gas diffusion losses in the fuel electrode.

cells are used for the air side. The higher frequency peak P4 is excluded, as it is assumed to be related to ionic transport at the GDC/YSZ interfaces which does not exhibit Butler-Volmer type behaviour.

Subsequently, the summed $R_{load,FE}$ and $R_{load,AE}$ (R_{diff} are subtracted from the total R_{pol}) are plotted over the current density. Both results can be fitted with a second-degree polynomial fit[31] as shown in Fig. 7c. The integration of the polynomial function with respect to current density helps calculate the current-dependent activation overpotentials $\eta_{act,\ FE}$ and $\eta_{act,\ AE}$.

$$\eta_{act,FE}(j) = \frac{1}{3}\cdot c_{11}\cdot j^3 + \frac{1}{2}\cdot c_{21}\cdot j^2 + c_{31}\cdot j + c_{41} \quad [13]$$

$$\eta_{act,AE}(j) = \frac{1}{3}\cdot c_{12}\cdot j^3 + \frac{1}{2}\cdot c_{22}\cdot j^2 + c_{32}\cdot j + c_{42} \quad [14]$$

After integrating these equations, the corresponding activation overpotentials for both electrodes are obtained using Eqs. 13 and 14. Using the boundary conditions (i.e., at OCV), the integration constants are computed to be zero. These curves were described using Butler-Volmer equation for both the electrodes. Thereby, with the help of MATLAB solver the calculated overpotentials are fitted to Butler-Volmer curves, yielding the charge transfer coefficients $\alpha_{FE} = 0.69$ and $\alpha_{AE} = 0.72$ as shown in Fig. 7d.

Peak identification.—A single DRT peak can be associated with multiple electrochemical processes occurring at both the fuel and air electrodes, making it challenging to pinpoint the exact physicochemical origins of each peak. To address this, we have summarized an approach that links these peaks to their respective origins, providing a structured overview of the key processes at both electrodes. The observations and calculations presented suggest that the overall polarization loss associated with the fuel electrode predominantly occurs in the frequency range below 10 Hz, while the air electrode's polarization loss is observed above 10 Hz. Based on the characteristic dependencies of the identified processes, a hypothesis regarding their physical origin has been proposed. Table III offers a comprehensive summary of elementary electrode reaction, the processes identified through DRT analysis, highlighting their characteristic frequency ranges, as well as their dependencies on gas partial pressure and temperature sensitivity.

Table V. Modeling parameters comparison for zero-dimensional cell model.

5.1 Fuel electrode				
Parameter	Unit	Value	Value[30]	Value[29]
Fuel Electrode	—	Ni/GDC (ESC A)	Ni/GDC (ESC B)	Ni/8YSZ (FESC)
(80% H_2, 20% H_2O)				
	eV	0.53	0.94	1.09
	Ωm^2	$5.74 \cdot 10^{-9}$	$2.95 \cdot 10^{-10}$	$3.83 \cdot 10^{-11}$
	—	0.22	0.16	0.1
	—	0.55	0.36	0.33
	$Am^{-2}K^{-1}$	$3.31 \cdot 10^{6}$	$8.88 \cdot 10^{7}$	$2.05 \cdot 10^{9}$
	—	0.69	0.76	0.59
5.2 Air electrode				
Parameter	Unit	Value	Value[30]	Value[29]
Air Electrode	—	LSM/composite (ESC A)	LSCF (ESC B)	LSCF (FESC)
(21% O_2, 79% N_2)				
	eV	1.47	1.50	1.45
	Ωm^2	$1.68 \cdot 10^{-12}$	$1.52 \cdot 10^{-14}$	$4.03 \cdot 10^{-13}$
	—	0.34	0.42	0.22
	$Am^{-2}K^{-1}$	$4.9 \cdot 10^{10}$	$6.14 \cdot 10^{12}$	$1.7 \cdot 10^{11}$
	—	0.72	0.65	0.65
5.3 Electrolyte				
Parameter	Unit	Value	Value[30]	Value[29]
Electrolyte	—	6ScSZ (ESC A)	3YSZ (ESC B)	8YSZ (FESC)
	eV	0.93	0.85	0.94
	Ωm^2	$8.72 \cdot 10^{11}$	$1.72 \cdot 10^{11}$	$4.19 \cdot 10^{12}$

Modeling and validation of the Current-Voltage characteristics.—To simulate the CV characteristics of the cell, the modeling approach setup by Leonide et al. was used.[29] Starting from the open circuit voltage, the cell voltage is determined by subtracting all the relevant losses including ohmic losses (discussed in A.2), activation losses at the fuel electrode (FE) and the air electrode (AE) as well as gas diffusion losses at both electrodes.[15]

$$U_{cell} = U_{OCV} - \eta_{ohm} - \eta_{act,FE} - \eta_{act,AE} - \eta_{diff,FE} - \eta_{diff,AE} \quad [15]$$

The developed model was further validated by comparing the simulation results with experimentally obtained data. Figure 8a presents the simulated and measured results across temperatures ranging from 900 °C to 750 °C, with a fuel gas mixture of 80% H_2 (balance H_2O) and air as oxidant. Minor deviations observed can be attributed to the self-heating of the cell, which is not considered in the isothermal 0Dmodel.[44] For the investigated conditions, the deviation Δ between simulated and measured data lies within the range of $0.01\% \leqslant \Delta \leqslant 5.13\%$.

The model is capable of simulating not only the CV-characteristics but also overpotentials associated with individual loss processes, as summarized in Fig. 8b. As expected for an ESC, ohmic losses have the highest contribution in cell performance. The model also shows high sensitivity to cell-specific constants and activation energies related to these ohmic losses.

Moreover, despite distinct dominant processes at fuel and air electrode, the overpotentials were nearly equal (15% and 21% respectively), with the air electrode showing a slightly higher overpotential (Fig. 8b). This can be expected, as the LSM air electrode is an electronic conductor, restricting the oxygen reduction reaction (ORR) to the triple-phase boundary (TPB), which reduces the effective reaction area and increases losses. As a result, while the mechanisms differ, the total impact on performance loss is similar for both electrodes.

Additionally, due to the thin electrodes, contacted by highly porous meshes, diffusion overpotentials are of least significance and can be considered negligible in the idealized single-cell test bench scenario. However, considering the transfer of this approach to a stack, a drastic increase in gas diffusion might occur if the cell is contacted by a metallic flow field via a thin contact layer.[45] In such cases, the in-plane gas diffusion beneath the contact ribs of the flow field geometry would significantly increase the effective diffusion length.

Comparison of performance.—Using the same model, a comparative analysis was conducted with two other cells - an ESC[30] and a FESC,[29] both previously analyzed in earlier studies (Fig. 9). This comparison supports the validity of the model across multiple cell architectures, demonstrating its applicability beyond a single configuration. The relevant parameters for comparison are summarized in Table IV.

Losses in different types of cells.—To compare the individual losses at the different electrodes, the simulation was run across a current density range from 0 to 1 A cm^{-2}. Diffusion, electrochemical, and ohmic overpotentials were calculated, using the published values for the other two cells. The simulations were conducted with similar gas compositions but at different temperatures corresponding to the nominal operating temperatures for the respective cell types: 850 °C for ESCs and 750 °C for FESC.

As expected, significant ohmic contributions are observed for both ESCs, with the difference largely attributed to the varying electrolyte materials such as 6ScSZ for the cell investigated in this study, and 3YSZ for the cell in Ref. 43. It is also evident that for the ESC´s, the fuel electrode's gas diffusion is approximately one order of magnitude smaller compared to the FESC. This difference is attributed to the gas diffusion in the porous Ni/YSZ-substrate of the FESC, which has a thickness of 1.5 mm,[29] whereas the overpotentials for gas diffusion polarization at the air electrodes are in a similar range. The state-of-the-art FESCs typically employ much thinner substrates—ranging from 300 to 500 μm—to minimize concentration overpotentials and enhance overall performance. Furthermore, the LSM air electrode contributes significantly and is a major part of the polarization losses in the investigated cell, whereas the fuel electrode has a relatively minor influence.

It is well-established in the literature that microstructure, electrode thickness, and temperature influence the performance of air electrodes quite differently.[23,46–48] Notably, the effects on SOEC performance are much smaller than on SOFCs, especially when the air electrode porosity is below 0.2 and the electrode thickness exceeds 100 μm.[23] Temperature also affects the two modes differently, with variations in porosity, particle diameter, thickness, and temperature being more significant in SOFCs than in SOECs. Additionally, the thickness of both the functional layer and current collector layer significantly influences electrochemical performance, further highlighting the complexity of optimizing cell performance based on these factors.[46] Therefore, to obtain more detailed results, future studies should focus on the microstructure (including particle diameter and porosity) and electrode thickness, as their effects on oxygen diffusion can vary significantly, particularly with thickness. However, as different electrodes in this study are manufactured by different industrial partners, further details regarding the microstructure are not available, resulting in limited results within this study.

Model parameters.—These calculated parameters are compared with those of other two cells previously tested in our laboratory and reported in the literature.[29,30] Detailed specifications of these cells are presented in Table V.

Conclusions

In this contribution, a well-established impedance spectroscopy-based analysis approach has been applied to an ESC with LSM-based air electrode. Polarization losses were evaluated through high-resolution impedance measurements across a broad range of operating conditions. The dependencies of individual cell components were systematically analyzed and interpreted based on ECM using DRT results followed by CNLS fit. The results indicate that ohmic resistance, including electrolyte losses, accounts for more than 60% of the total losses in the investigated cell. The primary polarization losses in the full cell were found to be associated with the electrochemical polarization of the LSM air electrode, which was modeled using RQ elements. In contrast, the contribution from gas diffusion (both air and fuel) was minimal (2%). This study highlights that the electrochemical performance of the ESC is predominantly influenced by the LSM air electrode.

Furthermore, a 0D stationary model was developed to predict the CV characteristics of planar ESCs. This model assists in predicting the losses and electrode behavior across a wide range of temperatures and gas compositions. The results show excellent agreement with experimentally obtained data, with deviations ranging from 0.01% to 5.13%. Additionally, a comparison was made using the same model across three cell types to investigate the differences between various electrode types. The results reveal that ohmic losses are predominant in ESCs, while diffusion losses dominate in FESCs. Moreover, LSM air electrodes and Ni/8YSZ fuel electrodes exhibit higher polarization losses compared to LSCF air electrodes and Ni/GDC fuel electrodes.

Acknowledgments

The authors gratefully acknowledge funding from the project "SOC Degradation 2.0" and the Federal Ministry of Education and Research (BMBF 03SF0621G). Sincere thanks are extended to the team at "former Hexis AG," particularly Dr Andreas Mai (Current affiliation: Celeroton AG, Volketswil 8604, Switzerland) and Dr Holger Bausinger (Current affiliation: Topsoe Germany GmbH, Essen 45130, Germany) for generously providing the cell samples investigated in this study.

Appendix

This section discusses the characterization of the full cell following the approaches outlined by Leonide et al.[29] and Grosselindemann et al.[30] EIS, combined with advanced modeling, is used to identify different loss mechanisms and develop a comprehensive understanding of the full cell.

Full Cells.—The first analysis involved a series of impedance measurements conducted on the full cell (ESC), with the corresponding DRTs presented in Fig. A·1.

Variation of temperature.—The DRTs derived from the impedance spectra of an ESC cell measured at different temperatures, ranging from 900 to 700 °C are shown in Fig. A·1. The impedance spectra were measured at two different fuel gas compositions: 95% H_2 (balance H_2O) and 40% H_2 (balance H_2O). At higher hydrogen content, as shown in Fig. A·1a, the low-frequency impedance significantly increases, adding one additional peak labeled as P1. The temperature dependency of P1, which is only visible at high temperatures, suggests a gas diffusion process at the fuel electrode. According to Eq. 3, this peak has a minimum when $pH_2 = pH_2O$ and increases with higher hydrogen or steam concentration. The spectra reveal a total of five peaks (P1 to P5) at higher hydrogen content, and four peaks at lower hydrogen content. Additionally, thermal activation is evident for all these peaks except P1, with the lower-frequency peak (P2) being the most strongly affected by temperature variations.

Variation of partial pressure.—To separate different electrochemical processes, variations were introduced by altering the partial pressure of steam ($p_{H2O,\ FE}$) in the fuel gas. N_2 was added as an inert gas component to the fuel gas mixture, while ambient air was used on the air side. The steam content was varied stepwise from 5% to 80%. Figure A·1c shows the DRTs computed from impedance spectra recorded at different compositions. The peak P1 displays a significant dependence on the steam content in the fuel gas, while peaks P2 and P3 show only minor dependencies. The influence of the steam content ($p_{H2O,\ FE}$) on the DRT demonstrates that peak P1 increases with lower steam content, implying higher gas diffusion at the fuel electrode.

Similarly, O_2 content in the air side gas mixture was varied from 21% (ambient air) to 1% (balance N_2), while keeping the composition of fuel-side composition constant (40% H_2, balance H_2O). The influence of the oxygen partial pressure ($p_{O2,\ AE}$) primarily affects the second peak (P2) in the DRT. At the same time, peak P3 shows only minor changes with variations in oxygen partial pressure.

The last two peaks (P4 and P5) exhibited minimal dependence on pressure but exhibited thermal activation behaviour. In the previous works[30,34] it has been mentioned that the contributions from grain bulk and boundaries appear in the high-frequency range and cannot be fully resolved. These contributions also become increasingly less visible at higher temperatures, and as a result, are typically not discussed in the literature. Consequently, the minor peaks P4 and P5 at higher frequencies (>1 kHz) are not considered in this electrochemical analysis.

This analysis clearly shows that the strong overlap of peaks related to both the air and fuel electrodes makes it difficult to conduct a detailed impedance analysis of full cells. The convolution of air and fuel electrode processes complicates the impedance data analysis, which are required for model parameterization. Since most model parameters can be determined under OCV conditions, the use of symmetrical cells is preferred for these studies.

Ohmic losses.—After determining the parameters for polarization losses, the ohmic losses resulting from electronic or ionic transport through the electrodes and the electrolyte were calculated, as described in Ref. 30. The total ohmic loss is the sum of individual contributions, including the area-specific resistance of the fuel and air electrodes, interlayer, electrolyte, and the interdiffusion layer. The electrolyte is designed to be dense to separate the air and fuel, exhibiting high oxygen ionic conductivity and negligible electronic conductivity, while remaining chemically and structurally stable over a wide range of conditions.

$$\eta_{ohm} = j \cdot R_{ohm} \qquad [A\cdot1]$$

To quantify these losses over a wide temperature range, the specific ohmic resistance was computed for a full cell, varying from 900 to 700 °C. The fuel electrode used a gas mixture of 80% H_2 (balance H_2O), while the air electrode used ambient air. The ohmic resistance values obtained from the CNLS fit were used for these calculations. As discussed in Ref. 3, ohmic losses dominate in an ESC, and thus a nonlinear description was necessary for their quantification. To account for the temperature dependency of ohmic activation energy, a parabola fit was applied to the measurement data. Using the approach from Ref. 30, the ohmic activation energy was extracted from the slope of the parabola, where the variable x is defined as $x = 1000\ \mathrm{K}\ \mathrm{T}^{-1}$, with K being the temperature in Kelvin.

$$E_{\mathrm{act,ohm}} = 1000\ \mathrm{K}\cdot\tilde{R}\left(2k_1 x + k_2 + \frac{1}{x}\right) \qquad [A\cdot2]$$

Subsequently, the cell specific parameter was derived, as described in Eq. A·3

$$B_{\mathrm{ohm}} = \frac{1000\mathrm{K}}{x}\cdot\exp\left(-\left(k_1 x^2 + k_2 x + k_3 - \frac{E_{\mathrm{act,ohm}}}{1000\mathrm{K}\cdot\tilde{R}}\cdot x\right)\right) \qquad [A\cdot3]$$

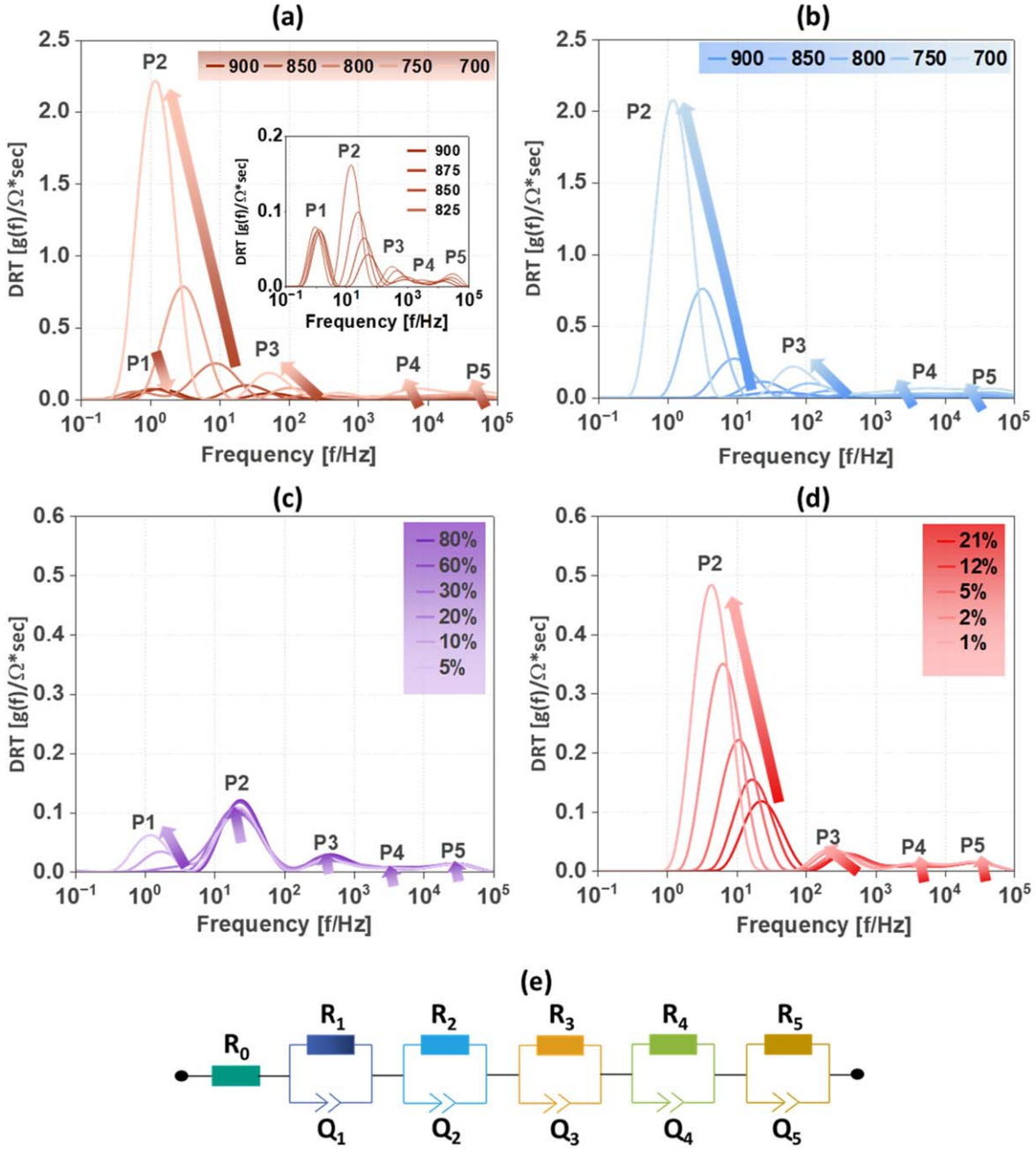

Figure A·1. DRTs of impedance spectra of an ESC full cell with Ni/GDC fuel electrode and LSM air electrode (a) fuel gas composition of 95% H_2 (balance H_2O) with air as an oxidant in a temperature range from 900 °C to 700 °C (b) fuel gas composition of 40% H_2 (balance H_2O) with air as an oxidant in a temperature range from 900 °C to 700 °C (c) variation of fuel gas composition (H_2 and H_2O balancing with N_2) at the fuel electrode with ambient air at the air electrode at 850 °C (d) variation of O_2 (balancing with N_2) at the air electrode with the fuel gas composition of 40% H_2 (balance H_2O) at the fuel electrode (e) Proposed equivalent circuit model for the electrochemistry of an ESC with Ni/GDC fuel electrode and LSM air electrode.

ORCID

S. Golani https://orcid.org/0000-0003-3715-1390
A. Weber https://orcid.org/0000-0003-1744-3732

References

1. K. Huang and J. B. Goodenough, *Solid Oxide Fuel Cell Technology, Principles, Performance and Operations* 11(Woodhead Publishing Ltd, Cambridge, United Kingdom) (2009).
2. J.-W. Kim et al., "Polarization effects in intermediate temperature, anode-supported solid oxide fuel cells." *J. Electrochem. Soc.*, **146**, 69 (1999).
3. S. Primdahl and M. Mogensen, "Gas diffusion impedance in characterization of solid oxide fuel cell anodes." *J. Electrochem. Soc.*, **146**, 2827 (1999).
4. P. Vinchhi et al., "Recent advances on electrolyte materials for SOFC: a review." *Inorg. Chem. Commun.*, **152**, 110724 (2023).
5. S. P. S. Badwal, "Zirconia-based solid electrolytes: microstructure, stability and ionic conductivity." *Solid State Ionics*, **52**, 23 (1992).
6. V. Vijaya Lakshmi et al., "Synthesis and characterization of nanocrystalline ScSZ electrolyte for SOFCs." *Int. J. Hydrogen Energy*, **36**, 14936 (2011).
7. D. Rembelski et al., "Characterization and comparison of different cathode materials for SC-SOFC: LSM, BSCF, SSC, and LSCF." *Fuel Cells*, **12**, 256 (2012).
8. S. P. Jiang et al., "Performance of GDC-impregnated Ni Anodes of SOFCs." *Electrochem. Solid-State Lett.*, **7**, A282 (2004).
9. S. P. Jiang et al., "Fabrication and performance of impregnated Ni anodes of solid oxide fuel cells." *J. Am. Ceram. Soc.*, **88**, 1779 (2005).
10. S. Zha, W. Rauch, and M. Liu, "Ni-Ce0.9Gd0.1O1.95 anode for GDC electrolyte-based low-temperature SOFCs." *Solid State Ionics*, **166**, 241 (2004).

11. A. Nenning et al., "Excellent kinetics of single-phase Gd-doped ceria fuel electrodes in solid oxide cells." *Materials Advances*, **2**, 5422 (2021).
12. V. A. Rojek-Wöckner et al., "A novel Ni/ceria-based anode for metal-supported solid oxide fuel cells." *J. Power Sources*, **328**, 65 (2016).
13. M. Riegraf et al., "Sulfur poisoning of electrochemical reformate conversion on nickel/gadolinium-doped ceria electrodes." *ACS Catal.*, **7**, 7760 (2017).
14. F. Thaler et al., "Redox stability of metal-supported fuel cells with nickel/gadolinium-doped ceria anode." *J. Power Sources*, **434**, 226751 (2019).
15. M. Riegraf et al., "Electrochemical impedance analysis of symmetrical ni/gadolinium-doped ceria (CGO10) electrodes in electrolyte-supported solid oxide cells." *J. Electrochem. Soc.*, **166**, F865 (2019).
16. M. P. Carpanese et al., "Understanding the electrochemical behaviour of LSM-based SOFC cathodes. Part I — Experimental and electrochemical." *Solid State Ionics*, **301**, 106 (2017).
17. D. Rembelski et al., "Characterization and comparison of different cathode materials for SC-SOFC: LSM, BSCF, SSC, and LSCF." *Fuel Cells*, **12**, 256 (2012).
18. E. P. Murray, T. Tsai, and S. A. Barnett, "Oxygen transfer processes in (La, Sr)MnO_3/Y_2O_3-stabilized ZrO_2 cathodes: an impedance spectroscopy study." *Solid State Ionics*, **110**, 235 (1998).
19. P. Moçoteguy and A. Brisse, "A review and comprehensive analysis of degradation mechanisms of solid oxide electrolysis cells." *Int. J. Hydrogen Energy*, **38**, 15887 (2013).
20. M. J. L. Østergård et al., "Manganite-zirconia composite cathodes for SOFC: influence of structure and composition." *Electrochim. Acta*, **40**, 1971 (1995).
21. A. Banerjee and O. Deutschmann, "Elementary kinetics of the oxygen reduction reaction on LSM-YSZ composite cathodes." *J. Catal.*, **346**, 30 (2017).
22. A. Mai et al., "Time-dependent performance of mixed-conducting SOFC cathodes." *Solid State Ionics*, **177**, 1965 (2006).
23. T. Tsai and S. A. Barnett, "Effect of LSM-YSZ cathode on thin-electrolyte solid oxide fuel cell performance." *Solid State Ionics*, **93**, 207 (1997).
24. M. Prestat and L. J. Gauckler, "Reaction pathways and kinetics of oxygen reduction at LSM cathodes." *ECS Proceedings Volumes*, **2001-16**, 574 (2001).
25. A. Barbucci et al., "Morphology and electrochemical activity of SOFC composite cathodes: I. experimental analysis." *J. Appl. Electrochem.*, **39**, 513 (2009).
26. A. Mai et al., "Progress in HEXIS' SOFC development." *ECS Trans.*, **91**, 63 (2019).
27. A. Mai et al., "Hexis and the SOFC system galileo 1000 N: experiences from lab and field testing." *ECS Trans.*, **68**, 109 (2015).
28. J. G. Grolig et al., "Development progress at hexis SOC activities." *ECS Trans.*, **103**, 275 (2021).
29. A. Leonide et al., "Evaluation and modeling of the cell resistance in anode-supported solid oxide fuel cells." *J. Electrochem. Soc.*, **155**, B36 (2008).
30. C. Grosselindemann et al., "Deconvolution of gas diffusion polarization in ni/gadolinium-doped ceria fuel electrodes." *J. Electrochem. Soc.*, **168**, 12 (2021).
31. A. Leonide, Y. Apel, and E. Ivers-Tiffée, "SOFC modeling and parameter identification by means of impedance spectroscopy." *ECS Trans.*, **19**, 81 (2009).
32. M. Schönleber, D. Klotz, and E. Ivers-Tiffée, "A method for improving the robustness of linear kramers-kronig validity tests." *Electrochim. Acta*, **131**, 20 (2014).
33. S. Dierickx, A. Weber, and E. Ivers-Tiffée, "How the distribution of relaxation times enhances complex equivalent circuit models for fuel cells." *Electrochim. Acta*, **355**, 136764 (2020).
34. S. Golani et al., "Impact of GDC interlayer microstructure on strontium zirconate interphase formation and cell performance." *J. Electrochem. Soc.*, **170**, 10 (2023).
35. F. Kullmann et al., "Impedance analysis of electrolyte processes in a solid oxide cell." *Fuel Cells*, **23**, 420 (2023).
36. M. Riegraf et al., "Electrochemical impedance analysis of NiCGO10-based electrolyte-supported cells." *ECS Trans.*, **91**, 1985 (2019).
37. C. Grosselindemann et al., "Comparison of a solid oxide cell with nickel/gadolinium-doped ceria fuel electrode during operation with hydrogen/steam and carbon monoxide/carbon dioxide." *Fuel Cells*, **23**, 442 (2023).
38. D. Esau et al., "Electrochemical characterization of nickel/gadolinia doped ceria fuel electrodes under H_2/H_2O/CO/CO_2-atmospheres." *J. Electrochem. Soc.*, **171**, 054522 (2024).
39. S. Liping et al., "La substituted Sr_2MnO_4 as a possible cathode material in SOFC." *J. Power Sources*, **179**, 96 (2008).
40. J. Kim et al., "Degradation mechanism of electrolyte and air electrode in solid oxide electrolysis cells operating at high polarization." *Int. J. Hydrogen Energy*, **38**, 1225 (2013).
41. J. Malzbender et al., "Component interactions after long-term operation of an SOFC stack with LSM cathode." *J. Power Sources*, **201**, 196 (2012).
42. S. Campanari and P. Iora, "Definition and sensitivity analysis of a finite volume SOFC model for a tubular cell geometry." *J. Power Sources*, **132**, 113 (2004).
43. D. Sánchez et al., "Thermal and electrochemical model of internal reforming solid oxide fuel cells with tubular geometry." *J. Power Sources*, **160**, 1074 (2006).
44. J.-C. Njodzefon et al., "Electrochemical modeling of the current-voltage characteristics of an SOFC in fuel cell and electrolyzer operation modes." *J. Electrochem. Soc.*, **160**, F313 (2013).
45. H. Geisler et al., "Stationary FEM model for performance evaluation of planar solid oxide fuel cells connected by metal interconnectors: I. model framework and validation." *J. Electrochem. Soc.*, **161**, F778 (2014).
46. W. Li et al., "Theoretical modeling of air electrode operating in SOFC mode and SOEC mode: the effects of microstructure and thickness." *Int. J. Hydrogen Energy*, **39**, 13738 (2014).
47. A. Barbucci et al., "Influence of electrode thickness on the performance of composite electrodes for SOFC." *J. Appl. Electrochem.*, **38**, 939 (2008).
48. V. A. C. Haanappel et al., "Optimisation of processing and microstructural parameters of LSM cathodes to improve the electrochemical performance of anode-supported SOFCs." *J. Power Sources*, **141**, 216 (2005).